Solid State Sciences 137 (2023) 107115

Contents lists available at ScienceDirect

Solid State Sciences

journal homepage: www.elsevier.com/locate/ssscie

Synthesis, crystal structure, optical, thermoelectric, and electrochemical studies of $Ba_2Cu_{2.1(1)}Ag_{1.9(1)}Se_5$

Gopabandhu Panigrahi, Subhendu Jana, Sadananda Muduli, Surendra K. Martha, Jai Prakash *

Department of Chemistry, Indian Institute of Technology Hyderabad, Kandi, Sangareddy, Telangana, 502284, India

ARTICLE INFO

Keywords:
Solid-state syntheses
Crystal structure
Thermoelectric properties
Supercapacitor

ABSTRACT

We present the synthesis and characterization of single crystals and polycrystalline samples of $Ba_2Cu_{2.1(1)}Ag_{1.9(1)}Se_5$. A single-crystal X-ray diffraction study confirms its monoclinic structure (space group: *C*2/*m*) with lattice parameters of $a = 16.0342(15)$ Å, $b = 4.4162(4)$ Å, $c = 9.1279(9)$ Å, $\beta = 124.005(2)^\circ$, $V = 535.82(9)$ Å^3 and $Z = 2$. The structure of $Ba_2Cu_{2.1(1)}Ag_{1.9(1)}Se_5$ consists of polyanionic $^2_\infty[Cu_{2.1(1)}Ag_{1.9(1)}Se_5]^{4-}$ layers. The negative charges on these layers are counterbalanced by the filling of Ba^{2+} cations in the structure. The Ag and Cu atoms are statistically disordered at the same sites. The Ag/Cu atoms are bonded with four Se atoms in a distorted tetrahedral fashion. The structure also contains linear Se_3^{4-} units with intermediate Se···Se interaction of 2.7734 (14) Å. The $Ba_2Cu_{2.1(1)}Ag_{1.9(1)}Se_5$ can be charge-balanced as $(Ba^{2+})_2(Cu^+)_{2.1}(Ag^+)_{1.9}(Se^{2-})_2(Se_3^{4-})_1$. The optical absorption study performed on a polycrystalline sample with a loaded composition of $Ba_2Cu_{2.1}Ag_{1.9}Se_5$ reveals a direct bandgap of 1.0(2) eV, and the indirect bandgap was found to be below 0.5 eV. The resistivity study also confirmed the semiconducting nature of the sample. The thermoelectric properties, including thermal conductivity and Seebeck coefficient, have been studied as a function of temperature. The polycrystalline $Ba_2Cu_{2.1}Ag_{1.9}Se_5$ has a very low thermal conductivity value of 0.46 W/mK at 673 K. The positive sign of the Seebeck coefficient values indicates the polycrystalline $Ba_2Cu_{2.1}Ag_{1.9}Se_5$ is a *p*-type semiconductor with holes as the majority of charge carriers. Further, the charge storage behavior of the material was investigated for supercapacitor application. The material delivers 76 F g^{-1} at 0.5 A g^{-1} current density in 1 M KOH electrolyte and is stable for 10,000 cycles retaining 85% capacitance.

1. Introduction

The catenation property of chalcogens (Q = S, Se, and Te), which helps these atoms to show hypervalency in various homochalcogen units, makes the structural chemistry of multinary metal chalcogenide more complex and richer compared to its oxide's counterpart. Typically, the complexity of chalcogenide structures can be enhanced by introducing more crystallographically independent cations in these structures; therefore, the structural and physical properties of quaternary chalcogenides are relatively more flexible and intriguing as compared to the binary or ternary counterparts. The chalcogenide structures featuring homoatomic bonding between Q atoms are commonly referred to as polychalcogenides. The average charge on the chalcogen atoms in the various Q_m^{n-} units varies depending on the shape of these homoatomic units and the bonding between the Q atoms. For instance, the $Ba_2Ag_4Se_2(Se_3)$ structure features unique linear Se_3^{4-} units, the $Ba_2Ag_2Se_2(Se_2)$ structure contains Se_2^{2-} dumbbells, and the Nb_2Se_9 structure is an example of a polychalogenide that has both Se_2^{2-} and Se_5^{4-} [1–3].

Transition metal-containing polychalcogenides have attracted solid-state and material research scientists for a long time due to their distinguished properties such as thermoelectric properties [4–6], transparent conductivity [7], high-temperature superconductivity [8–10], magnetism [11,12], charge density wave [13], catalytic [14], and non-linear optics [15]. As described earlier, the self-catenation nature of the chalcogens in these structures enhances the structural complexity of metal polychalcogenide, and hence these structures adopt a variety of structure types that vary from zero-dimensional to three-dimensional. The main motivation for exploring new metal chalcogenides with narrow bandgaps in the last decade has arisen due to their potential thermoelectric applications. The development of electrical power generators, which have the ability to produce electrical energy from the waste heat produced from industries, power plants,

* Corresponding author..
E-mail address: jaiprakash@chy.iith.ac.in (J. Prakash).

https://doi.org/10.1016/j.solidstatesciences.2023.107115
Received 6 October 2022; Received in revised form 9 December 2022; Accepted 16 January 2023
Available online 18 January 2023

internal combustion engines, etc., is crucial to make use of fossil fuels efficiently. Thermoelectric (*TE*) materials can also be used in cooling devices, which only use electrical current to operate [16]. These *TE* coolers are more reliable due to the lack of any moving parts. Thermoelectric properties of many transition metal-containing chalcogenides were studied in the mid or high-temperature range such as $Cu_{2-x}Se$ [17], doped-$AgSbTe_2$ [18], $BaCu_2Se_2$ [19], $Ba_3Cu_{14-\delta}Te_{12}$ [20], $AgBi_3S_5$ [21], and $AgBiSe_2$ [22]. Many transition metal-containing chalcogenides usually have layered two-dimensional or quasi-two-dimensional structures, and specific properties of these layered chalcogenides originate from these layers [7]. Another important application of metal chalcogenide-based materials is to use them as high-performance metal ion capacitors due to their high performance and high energy efficiency [23]. In this perspective, predominantly binary transition metal chalcogenides have been explored in the literature, and complex ternary and quaternary transition metal chalcogenides are largely overlooked for ion capacitor applications.

We have been exploring the ternary and quaternary Cu/Ag-containing chalcogenides, mainly for *TE* applications. Our exploration has yielded a few new ternary and quaternary compounds like $BaAgSe_2$, $BaM_{1-x}Te_2$, $BaScMQ_3$ (M = Cu and Ag; Q = Se and Te), and $Ba_3Zr_2Cu_4S_9$ [2,24–26]. In this article, we report the synthesis of the non-stoichiometric pseudo quaternary selenide $Ba_2Cu_{2.1(1)}Ag_{1.9(1)}Se_5$ of the Ba–Cu–Ag–Se system. The Cu and Ag atoms are mixed at the same sites as established by the single-crystal X-ray diffraction study. The phase pure polycrystalline sample with the loaded composition $Ba_2Cu_{2.1}Ag_{1.9}Se_5$ was synthesized for the first time and used to investigate its physical properties, such as optical, temperature-dependent resistivity, and thermoelectric properties. Moreover, we have also examined the electrochemical properties of the polycrystalline $Ba_2Cu_{2.1}Ag_{1.9}Se_5$ sample for supercapacitor application.

2. Experimental

2.1. Materials used and synthesis

The following reactants were used as received for the synthesis of $Ba_2Cu_{2.1(1)}Ag_{1.9(1)}Se_5$: barium rod (Alfa Aesar, 99+%), silver flakes (Sigma-Aldrich, >99.9%), copper powder (Alfa Aesar, 99.98%), and selenium powder (Sigma-Aldrich, 99.5%). These chemicals were stored and handled inside an argon-filled dry glove box to avoid oxidation.

2.1.1. Synthesis of single crystals of $Ba_2Cu_{2.1(1)}Ag_{1.9(1)}Se_5$

The black-colored crystals of $Ba_2Cu_{2.1(1)}Ag_{1.9(1)}Se_5$ were obtained by exploratory solid-state synthesis carried out in the Ba–Cu–Ag–Se system. The target composition was $Ba_2Cu_2Ag_2Se_5$. A reaction mixture of Ba (54.2 mg, 0.395 mmol), Ag (42.6 mg, 0.395 mmol), Cu (25.1 mg, 0.395 mmol), and Se (78.0 mg, 0.987 mmol) were first transferred in a carbon-coated sealed fused silica tube (having an outer diameter of 6 mm). The tube was then sealed under the vacuum (*ca.* 10^{-4} Torr) with the help of a flame torch. The sealed tube was placed inside a programmable furnace. The temperature of the furnace was ramped to 873 K from room temperature (RT) in 12 h, where the reaction mixture dwelled for 96 h. The tube was then slowly cooled down to 373 K at a rate of 5 K/h to felicitate the crystal growth. Finally, the furnace was switched off and radiatively cooled to RT.

The elemental compositions of the crystals obtained from the reaction product were studied using an octane elite energy dispersive X-ray spectrometer (EDX) (EDAX Inc, USA) that was attached to a field-emission scanning electron microscope (FE-SEM) (Make: JEOL, Japan; Model: JSM 7800F). The EDX data were collected on a few black-colored crystals at random points with an accelerating voltage of 15-20 kV. The semi-quantitative EDX analysis confirmed the presence of four elements, Ba, Cu, Ag, and Se, in these black crystals. The compositions of these black crystals were consistent with $\approx Ba_2Cu_{2.1}Ag_{1.9}Se_5$ composition. The EDX area mapping of a typical crystal of $Ba_2Cu_{2.1(1)}Ag_{1.9(1)}Se_5$ is shown in Fig. 1a, which shows the homogenous distribution of all the four elements with $Ba_{20.5(2)}Cu_{21.4(6)}Ag_{18.9(5)}Se_{52.8(8)}$ composition.

The sizes of these black crystals are in the range of about 200–400 μm in length and 10–50 μm in width. The EDX study did not detect any trace of silicon/oxygen in these black crystals of $Ba_2Cu_{2.1(1)}Ag_{1.9(1)}Se_5$.

2.1.2. Synthesis of the polycrystalline $Ba_2Cu_{2.1}Ag_{1.9}Se_5$

After establishing the composition and crystal structure of $Ba_2Cu_{2.1(1)}Ag_{1.9(1)}Se_5$, a polycrystalline sample with a loaded composition of $Ba_2Cu_{2.1}Ag_{1.9}Se_5$ was synthesized using the sealed tube solid-state method. The stoichiometric amounts of Ba, Cu, Ag, and Se consistent with $Ba_2Cu_{2.1}Ag_{1.9}Se_5$ composition were loaded inside a carbon-coated fused silica tube having a 10 mm inner diameter and 12 mm outer diameter inside the argon-filled glove box. The fused silica tube containing the reaction mixture was evacuated (*ca.* 10^{-4} Torr) and then sealed using the flame torch. The sealed ampoule was placed inside the furnace, and the temperature was slowly ramped up to 823 K with a heating rate of ~83 K/h. The reaction mixture was annealed at 823 K for 24 h to react the metals with Se. Subsequently, the temperature was again ramped up to 1023 K (above the melting point of Ba) at a rate of ~63 K/h, and the reaction mixture was dwelled for 24 h before switching off the furnace. A black lump formed in the first step was ground inside the Ar-filled glove box, pressed into cylindrical pellets, and reheated in a sealed fused silica tube at 823 K for 72 h. The sintered pellets were characterized by a powder X-ray diffraction study.

2.2. Single-crystal X-ray diffraction study

Single-crystal X-ray diffraction data of $Ba_2Cu_{2.1(1)}Ag_{1.9(1)}Se_5$ were collected at 298(2) K using a Bruker D8 Venture instrument equipped with a Photon-III mixed mode detector. A graphite monochromatized Mo-$K\alpha$ radiation with a wavelength of 0.71073 Å was used for the diffraction experiment. The EDX-analyzed crystals were picked under N-paratone oil and used for unit cell determination. The unit cell constants of several black crystals were checked by the fast scan. The refined cell constants were found to be very similar for these crystals indicating a narrow homogeneity range of Cu/Ag content in the crystals. The working voltage and operating currents were 50 kV and 1.5 mA, respectively, throughout the experiment. The distance between the X-ray detector and the crystal was fixed at 5 cm. The intensity data were collected as a series of 0.5° frame width in ω and ϕ scans, and each frame was collected with an exposure time of 2 s. The APEX3 software [27] package was used for data collection, cell refinement, and data reduction. The absorption corrections of the measured reflections were done by the multiscan method implemented in the SADABS [28] program.

The crystal structure of $Ba_2Cu_{2.1(1)}Ag_{1.9(1)}Se_5$ was solved and refined using the SHELX-14 suite of programs [29]. The XPREP program [30] suggested monoclinic symmetry with the *C*-centering of the cell. The three space groups [*C*2 (no. 5), *C*2/*m* (no. 12), and *Cm* (no. 8)] consistent with the observed reflection's extinction condition were identified by the XPREP program. The statistics of intensity ($|E^2 - 1| = 0.843$) favored a centrosymmetric structure. Hence, the centrosymmetric monoclinic *C*2/*m* (no. 12) space group was chosen for the structure solution. The initial model of the crystal structure of the $Ba_2Cu_{2.1(1)}Ag_{1.9(1)}Se_5$ was obtained by the direct methods using the SHELXS program [31] that identified six crystallographic independent atomic positions. These positions were initially assigned as one Ba, two Ag, and three Se sites. The subsequent refinement of the structure reveals that both of the transition metal sites were mixed (Ag/Cu). The Ag and Cu atoms were allowed to have the same fractional atomic coordinates by using the EXYZ constraints. The site occupancy factor (SOF) values of Ag and Cu were refined freely, and their anisotropic thermal parameters were kept the same using the EADP constraint. The ADDSYM [32] program of the PLATON [32] also agreed with the solved model and did not suggest any higher symmetric space group for the final structure. Mixing Ag/Cu at the same sites yielded significantly lower values of crystallographic

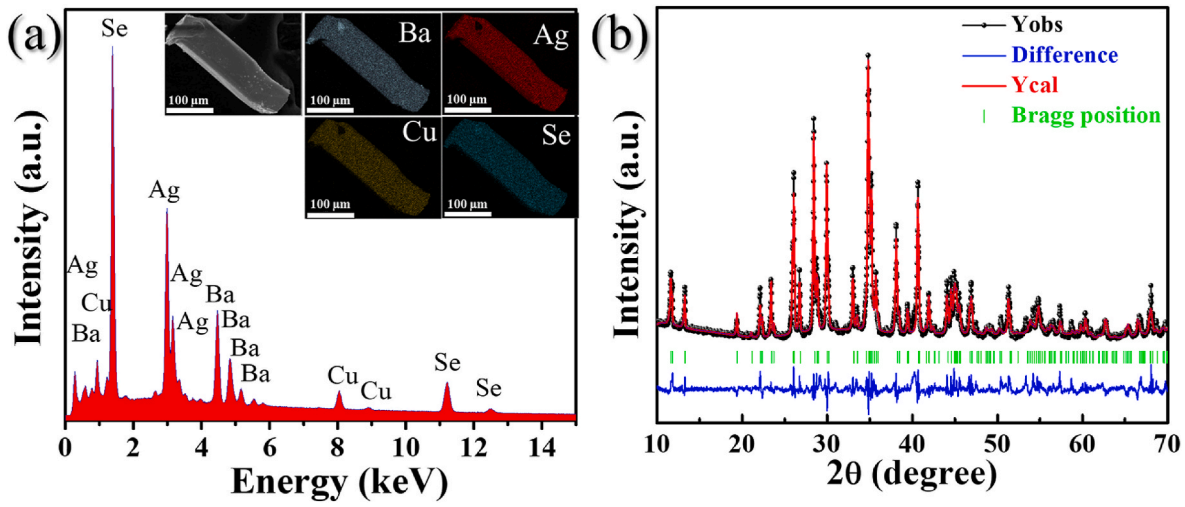

Fig. 1. (a) The EDX spectrum and area mapping (inset) of the $Ba_{20.5(2)}Cu_{21.4(6)}Ag_{18.9(5)}Se_{52.8(8)}$ crystal and **(b)** the Le Bail refinement of an experimental PXRD data of the polycrystalline sample with the loaded composition of $Ba_2Cu_{2.1}Ag_{1.9}Se_5$. The experimental X-ray pattern, Bragg positions of reflections, calculated pattern, and the difference plot are depicted as solid black dots, green ticks, solid red line, and solid blue line, respectively. The R_{exp}, R_{wp}, R_p, and goodness of fit (χ) values are 2.95%, 8.63%, 6.51%, and 2.93, respectively.

reliability factors [$R(F)$ and $R_w(F_o^2)$]. The $M1$ (Cu1+Ag1) disordered site contains a slight excess of copper (~10%) as compared to the Ag atom, whereas the $M2$ site has nearly equal amounts of Ag and Cu (Ag = 49.3% and Cu = 50.07%). The formula obtained after final refinements is $Ba_2Cu_{2.1(1)}Ag_{1.9(1)}Se_5$ ($Z = 2$). Finally, the parameters like scale factors, atomic positions with anisotropic displacement parameters, and extinction parameters were refined. The atomic positions were at last standardized using the program STRUCTURE TIDY [33]. Further details of structure refinement and crystallographic parameters are provided in Tables 1–3 and in the supporting information (SI) file.

2.3. Powder X-ray diffraction (PXRD) study

The phase purity of the polycrystalline reaction products was evaluated by the PXRD studies. The PXRD data of the finely ground samples were collected at RT using a Rigaku Ultima IV diffractometer with Cu-$K\alpha$ radiation ($\lambda = 1.5406$ Å) source. The PXRD data were recorded over a 2θ range of 10°–70° using a θ-2θ geometry. The experimental PXRD patterns were compared with the calculated PXRD patterns simulated from the single-crystal structural data. The PXRD patterns were analyzed using the *Match3!* software [34].

Table 1
Crystallographic data and structure refinement details for $Ba_2Cu_{2.1(1)}Ag_{1.9(1)}Se_5$ structure.[a]

Chemical formula	$Ba_2Cu_{2.1(1)}Ag_{1.9(1)}Se_5$
Space group	$C_{2h}^3 - C2/m$
a (Å)	16.0342(15)
b (Å)	4.4162(4)
c (Å)	9.1279(9)
β (°)	124.005(3)
V (Å^3)	535.82(9)
Z	2
ρ (g cm^{-3})	6.244
μ (mm^{-1})	31.64
$R(F)$[b]	0.047
$R_w(F_o^2)$[c]	0.107

[a] $\lambda = 0.71073$ Å, $T = 298(2)$ K.
[b] $R(F) = \Sigma\ ||F_o|-|F_c||/\Sigma|F_o|$ for $F_o^2 > 2\sigma(F_o^2)$.
[c] $R_w(F_o^2) = \{\Sigma\ [w(F_o^2 - F_c^2)^2]/\Sigma wF_o^4\}^{1/2}$. For $F_o^2 < 0$, $w = 1/[\sigma^2(F_o^2) + (0.0074P)^2 + 41.9620P]$ where $P = (F_o^2 + 2F_c^2)/3$.

2.4. UV–visible–near infrared (UV–vis–NIR) absorption study

The optical bandgap study of the polycrystalline sample with the loaded composition of $Ba_2Cu_{2.1}Ag_{1.9}Se_5$ was carried out at RT. The polycrystalline sample was homogenized into a fine powder inside the Ar-filled glove box before using it for collecting the UV–vis–NIR data. The absorption study was carried out using a JASCO V-770 UV/VIS/NIR spectrophotometer instrument against a $BaSO_4$ standard, over the wavelength range of 2500 nm (~0.5 eV) to 354 nm (3.5 eV). The Kubelka–Munk equation, $\alpha/S = (1 - R)^2/2R$, was used to transform the reflectance data into absorption data. Here α, S, and R are the absorption coefficient, scattering coefficient, and reflectance, respectively [35].

2.5. Thermal conductivity measurement of the polycrystalline $Ba_2Cu_{2.1}Ag_{1.9}Se_5$

The thermal conductivity study of the polycrystalline $Ba_2Cu_{2.1}Ag_{1.9}Se_5$ sample was done on a cylindrical (8 mm dia.) dense cold-pressed pellet with the help of a Linseis Xenon Flash (XFA 500) thermal diffusivity measurement system. The details of the thermal diffusivity measurements are given elsewhere [25]. The following equation was used to calculate the thermal conductivity of the sample:

$$k_{total} = d \times D \times C_p. \quad (1)$$

Here k_{total}, d, D, and C_p are total thermal conductivity, the density of the cylindrical pellet, thermal diffusivity, and heat capacity of the sample, respectively. The $Ba_2Cu_{2.1}Ag_{1.9}Se_5$ pellet was coated with a thin layer of graphite before performing the thermal diffusivity experiment to reduce the radiative heat loss. The thermal conductivity data were recorded over a temperature range of 373 K–673 K. The Dulong-petit law of heat capacity was used to calculate heat capacity [36], and the density of the sample was calculated by the Archimedes principle. The density of the pellet was about 93% of the theoretical density obtained by the single-crystal study. The total thermal conductivity was calculated using equation (i). The thermal conductivity values are associated with an instrumental error of about 10%. The PXRD study of the sample showed no sign of oxidation or phase degradation after the experiment. Thus, the sample is stable under the measured conditions. Also, the thermal diffusivity data of heating and cooling cycles were in good agreement within the experimental error.

Table 2
Fractional atomic coordinates and U_{iso}/U_{eq} values[a] for the $Ba_2Cu_{2.1(1)}Ag_{1.9(1)}Se_5$ structure.

	Wyckoff position	Site symmetry	SOF	*x*	*y*	*z*	U_{iso}*/U_{eq}[a]
Ba1	4*i*	*m*	1	0.31015(5)	0.000000	0.31619(10)	0.0212(2)
Cu1	4*i*	*m*	0.55(2)	0.06028(13)	0.000000	0.2314(4)	0.0589(9)
Ag1	4*i*	*m*	0.45(2)	0.06028(13)	0.000000	0.2314(4)	0.0589(9)
Cu2	4*i*	*m*	0.51(2)	0.42582(14)	0.000000	0.0425(2)	0.0400(6)
Ag2	4*i*	*m*	0.49(2)	0.42582(14)	0.000000	0.0425(2)	0.0400(6)
Se1	4*i*	*m*	1	0.12248(11)	0.000000	0.86633(19)	0.0285(3)
Se2	4*i*	*m*	1	0.64891(11)	0.000000	0.2880(2)	0.0274(3)
Se3	2*c*	2/*m*	1	0.000000	0.000000	0.500000	0.0300(5)

[a] U_{iso}/U_{eq} is the one-third value of the trace of orthogonalized U_{ij} tensor.

Table 3
Selected interatomic distances (Å) for the $Ba_2Cu_{2.1(1)}Ag_{1.9(1)}Se_5$ structure.

Atomic pair	Bond Distances (Å)	Atomic pair	Bond Distances (Å)
[a]*M*1−Se1	2.541(2)	Ba1–Se1	3.2910(12) × 2
*M*1−Se2	2.5181(11) × 2	Ba1–Se1	3.4779(17)
*M*1−Se3	3.098(2)	Ba1–Se2	3.2910(17)
*M*2−Se1	2.6249(12) × 2	Ba1–Se2	3.2989(11) × 2
*M*2−Se2	2.548(2)	Ba1–Se3	3.3532(6) × 2
*M*2−Se2	2.975(2)	Ba1···*M*1	3.630(1)
*M*1···*M*1	3.528(1)	Ba1···*M*2	3.856(1)
*M*2···*M*2	2.885(1)	*M*1···*M*2	2.888(1)
Se···Se	2.773(1)	-	–

[a] *M* = Ag/Cu.

2.6. Seebeck coefficient and electrical resistivity of the polycrystalline $Ba_2Cu_{2.1}Ag_{1.9}Se_5$

The temperature dependence of the Seebeck coefficient (*S*) and electrical resistivity (ρ) values were studied by using a ULVAC-RIKO ZEM-3 instrument to evaluate the thermoelectric figure of merit (zT) for the polycrystalline $Ba_2Cu_{2.1}Ag_{1.9}Se_5$. The efficiency of a *TE* material is measured by its zT value [= $(S^2\sigma/k_{total})T$], which is inversely proportional to the total thermal conductivity (k_{total}) and directly proportional to the *S* and electrical conductivity (σ) value. The electrical resistivity is the inverse of the σ value.

The values of electrical resistivity and Seebeck coefficient were collected for the sample as a function of temperature under a helium atmosphere. The experiment was performed on a compact parallelepiped pellet having dimensions of 12 mm × 6 mm × 2.5 mm. The pellet was fabricated from the polycrystalline powder sample under the pressure of ~15 MPa and sintered at 773 K for 24 h in a carbon-coated sealed tube. The electrodes were cleaned properly before collecting the data to avoid errors. The error associated with the electrical resistivity and Seebeck coefficient values is about 5%.

2.7. Electrochemical characterizations

Electrodes were prepared by coating the active material (i.e., polycrystalline $Ba_2Cu_{2.1}Ag_{1.9}Se_5$) slurry (~4 mg cm^{-2}) onto a graphite sheet (1 cm^2 area) current collector and dried at 363 K overnight under vacuum for electrochemical studies. The slurry was prepared by using 80% of $Ba_2Cu_{2.1}Ag_{1.9}Se_5$ active material, 10% polyvinylidene difluoride binder (99.5%, Sigma-Aldrich), and 10% of carbon black (Super P-65) in N-methyl pyrrolidone (99%, Sigma-Aldrich).

Composite electrodes' electrochemical performances were studied using galvanostatic charge-discharge (GCD) cycling, cyclic voltammetry (CV), and electrochemical impedance spectroscopic (EIS) studies. The electrochemical characteristics were studied using a three-electrode setup containing a platinum counter electrode and a saturated calomel reference electrode in the potential range between −0.8 and 0.5 V in 1 M KOH electrolyte. All these experiments were analyzed using a cell test system (Solartron analytical, Oak Ridge, TN, USA) model 1470E coupled with an FRA model 1455A. The EIS responses were recorded within a frequency range of 1 MHz and 10 mHz at an amplitude of 5 mV under the fully discharged condition. Further, the obtained EIS data were analyzed using Z-view software (Scribner Associates, USA).

The composite electrodes' electrochemical specific capacitance (C_s) was calculated from GCD curves using the following equation [37,38].

$$C_s = \frac{I\Delta t}{m\Delta V}\ \mathrm{F\ g^{-1}} \quad (2)$$

where I (A) is current, m (g) is the mass of active material, Δt (s) is discharge time, and ΔV (V) is the voltage window of the measurement.

3. Results and discussion

3.1. Synthesis and crystal structure of $Ba_2Cu_{2.1(1)}Ag_{1.9(1)}Se_5$

The black-colored crystals of quaternary $Ba_2Cu_{2.1(1)}Ag_{1.9(1)}Se_5$ were first synthesized by the high-temperature reaction of elements at 873 K. The approximate yield of $Ba_2Cu_{2.1(1)}Ag_{1.9(1)}Se_5$ crystals was about 30% based on the silver. A series of reactions involving Ba, Ag, Cu, and Se elements with the loaded compositions of $Ba_2Cu_{2.1}Ag_{1.9}Se_5$ was carried out with varying temperature profiles to optimize the reaction conditions to obtain a monophasic polycrystalline sample. The phase pure polycrystalline sample of $Ba_2Cu_{2.1}Ag_{1.9}Se_5$ was obtained by the stoichiometric reaction of corresponding elements at high temperatures using a two-step method. First, the reactants were heated at 1023 K for 24 h to produce a homogenized black lump that was compacted into a disk. This disk was again reheated at 873 K in the second step to make polycrystalline $Ba_2Cu_{2.1}Ag_{1.9}Se_5$ powder. The phase purity of the homogenized polycrystalline sample was confirmed by the Le bail refinement of the experimental PXRD data using the TOPAS software package [39] (Fig. 1b). The refined cell constants of a = 16.042(1) Å, b = 4.428 (1) Å, c = 9.141(1) Å, and β = 123.903(1)° agree well with the constants calculated by the SCXRD study. The homogeneity limit of Cu in the $Ba_2Cu_{2.1(1)}Ag_{1.9(1)}Se_5$ structure was not studied and is out of the scope of this work.

3.1.1. Crystal structure of $Ba_2Cu_{2.1(1)}Ag_{1.9(1)}Se_5$

Fig. 2 shows the crystal structure of $Ba_2Cu_{2.1(1)}Ag_{1.9(1)}Se_5$ as determined by the single-crystal X-ray diffraction study at 298(2) K. The transition metals in this structure are disordered. The $Ba_2Cu_{2.1(1)}Ag_{1.9(1)}Se_5$ crystallizes in the monoclinic C^3_{2h} −*C*2/*m* space group with two formula units (*Z*) per unit cell. The refined cell constants for the structure are a = 16.0342(15) Å, b = 4.4162(4) Å, c = 9.1279(9) Å, β = 124.005 (2)°, and V = 535.82(9) $Å^3$. This structure belongs to the $Ba_2Ag_4Se_5$ structure type first reported by Assoud *et al.* [1]. The same group also attempted to make Cu-analogue, *i.e.*, $Ba_2Cu_4Se_5$, without any success. However, they could synthesize two solid solutions with the general formula $Ba_2Cu_\delta Ag_{4-\delta}Se_5$: $Ba_2Cu_{0.88(7)}Ag_{3.12}Se_5$ (V = 550.5(1) $Å^3$) and $Ba_2Cu_{1.78(7)}Ag_{2.22}Se_5$ (V = 539.93(9) $Å^3$). Their studies concluded that the homogeneity limit of Cu substitution is below δ = 2. The unit cell volume of the $Ba_2Cu_{2.1(1)}Ag_{1.9(1)}Se_5$ is slightly smaller than the $Ba_2Cu_{1.78(7)}Ag_{2.22}Se_5$ phase, which could be attributed to more concentration of Cu in the structure which is smaller than the Ag atom.

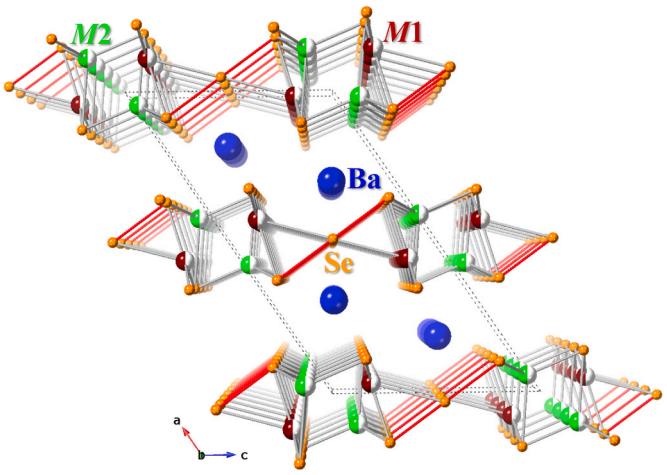

Fig. 2. A perspective view of the unit cell of the $Ba_2Cu_{2.1(1)}Ag_{1.9(1)}Se_5$ structure along the *b*-axis. The Se···Se interactions of 2.7734(14) Å are shown as solid red lines. The Ba–Se interactions are omitted for clarity.

The asymmetric unit of the $Ba_2Cu_{2.1(1)}Ag_{1.9(1)}Se_5$ structure comprises six independent crystallographic sites: one Ba1, one *M*1, one *M*2, and three Se sites (Se1, Se2, and Se3). The *M*1 and *M*2 indicate the mixed Ag/Cu sites. All these atoms are situated on the mirror plane, but Se3 has a site symmetry of 2/*m* (Table 2). The overall crystal structure of $Ba_2Cu_{2.1(1)}Ag_{1.9(1)}Se_5$ can be described as pseudo-two-dimensional, as depicted in Fig. 2.

The Ba atoms in this structure are predominantly electron donors and involved in non-directional ionic interactions with the neighboring Se atoms. Thus the structure can be seen as a combination of anionic layers of $^2_\infty[Cu_{2.1(1)}Ag_{1.9(1)}Se_5]^{4-}$ that are charge-balanced by the Ba^{2+} cations, which are held in between the two anionic layers (Fig. 2). The mixed *M*1 and *M*2 atoms in this structure sit at the center of distorted tetrahedra made up of four Se atoms. The *M*1−*M*2 distance is 2.8876(2) Å, which is longer than the Cu–Cu or Ag–Ag distance observed in the elemental Cu or Ag structures [40,41]. The *M*1−Se and *M*2−Se distances range from 2.518(2)−3.0976(2) Å and 2.548(2)–2.975(2) Å, respectively. The *M*1–Se3 (3.0976(2) Å) bond in the *M*1Se_4 tetrahedra is elongated. Similarly, the *M*2Se_4 unit also contains an elongated *M*2–Se2 pair (2.975(2) Å). Due to the presence of slight excess of Cu in the $Ba_2Cu_{2.1(1)}Ag_{1.9(1)}Se_5$ structure than the earlier reported $Ba_2Cu_{1.78(7)}Ag_{2.22}Se_5$ compound [1], the *M*1−Se and *M*2−Se bond lengths in the former structure are slightly shorter than that of the latter structure.

The Se3 atoms, which are part of the *M*1Se_4 tetrahedra, play an important role in stabilizing the 2D layers of $^2_\infty[Cu_{2.1(1)}Ag_{1.9(1)}Se_5]^{4-}$. The Se3 atoms act as a bridge between two one-dimensional clusters made up of [*M*1*M*2Se1Se2] that extend in the *b*-direction, as shown in Fig. 3a. As a result of this, the Se3 and Se1 atoms form linear trimers of Se1···Se3···Se1 with a bond angle of 180° and Se1···Se3 interactions of 2.7734(14) Å. These Se1···Se3 interactions are longer than the classical single Se···Se bond of ~2.4 Å [42] but are shorter than the van der Waals interactions (3.8 Å) between two Se atoms. This implies that the bonding in the Se1···Se3···Se1 trimers can't be explained on the classical 2c−2e$^-$ bonding.

The partition of charges to the individual atom is not straightforward in the $Ba_2Cu_{2.1(1)}Ag_{1.9(1)}Se_5$ structure due to Se1···Se3···Se1 interactions. The formula can be written as $Ba_2Cu_{2.1(1)}Ag_{1.9(1)}$ $(Se1)_2(Se2)_2(Se3)_1$ to understand the assignment of charges on the Se atoms. The charges on metals Ba and Cu (or Ag) can be assigned as +2 and + 1, respectively. Each Se2 atom has a charge of −2 since it does not involve in any homoatomic interaction. This assignment leaves a total negative charge of −4 on 2Se1+Se3 atoms. As evident, there are two different types of Se atoms (Se1 and Se3) present in the Se_3 trimers; Se1 is involved in terminal bonding interaction with Cu/Ag metal and is expected to have a charge of −2, and the Se3 atom sits at the center of the trimer. Both ends of the trimer are connected with Cu/Ag atoms in *M*1···Se1···Se3···Se1···*M*1 sequence where 4e$^-$ are delocalized over three Se atoms forming a hypervalent 3c−4e$^-$ bond. Thus the Se trimer can be represented as Se_3^{4-} units and charge-balanced composition can be formulated as $(Ba^{2+})_2(Cu^+)_{2.1}(Ag^+)_{1.9}(Se^{2-})_2(Se_3^{4-})_1$ as per the Zintl-Klemm concept.

The hypervalent Se_3^{4-} is isoelectronic with the well-known I_3^- anion and Sb_3^{7-} unit found in $Ca_{13}LnMnSb_{11}$ (*Ln* = lanthanides) [43]. There are a few well-known examples of metal selenides that contain Se_3 trimers with different bond angles and Se–Se interactions. One such compound is $Rb_{12}Nb_6Se_{35}$ [44], where the Se–Se–Se bond angles in the Se_3 trimers are in the range of 163°–164° and Se···Se interactions are 2.59(1)−2.64 (1) Å. The Se_3 trimer unit of the $K_3CuNb_2Se_{12}$ structure has a bond angle of 166°, and Se–Se interaction varies from 2.726(3)–2.542(3) Å [45], and in the Nb_2Se_9 structure, the bond angle in the trimer units is 83.5° with Se–Se interaction of 2.364(2)–2.663(2) Å [3]. Although $Rb_{12}Nb_6Se_{35}$ and Nb_2Se_9 structures contain hypervalent Se_3^{4-} units, but their geometries are not linear, unlike $Ba_2Ag_4Se_5$ [1] and $Ba_4Cu_8Se_{13}$ [46] structures, which contain linear Se_3 trimers (bond angle of 180°) and Se–Se interaction of ~2.77 Å. The thermal ellipsoid of the Se3 atoms in the $Ba_2Cu_{2.1(1)}Ag_{1.9(1)}Se_5$ structure is slightly elongated (Fig. 3b) along the bond axis, as shown in Fig. 3b, which suggests that the Se3 atoms vibrate more than the Se1 atoms in the Se_3^{4-} units.

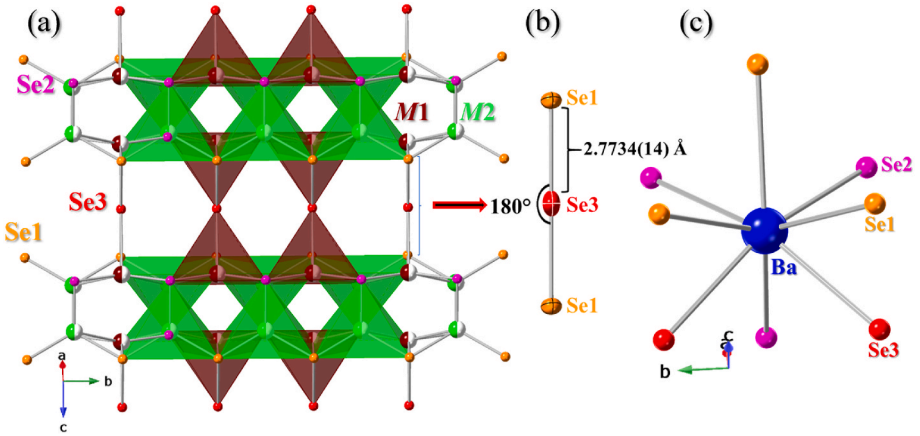

Fig. 3. (a) A fragment of the anionic layer of $^2_\infty[Cu_{2.1(1)}Ag_{1.9(1)}Se_5]^{4-}$, **(b)** a schematic representation of the hypervalent bonding in Se_3^{4-} showing the slight elongation of the thermal ellipsoid (shown at 50% probability level) of the Se3 atom along the bond axis, and (c) the coordination environment of the Ba atom in $Ba_2Cu_{2.1(1)}Ag_{1.9(1)}Se_5$ structure.

The Ba atoms in the structure are coordinated with eight Se (three Se1, three Se2, and two Se3) atoms that form a distorted square antiprismatic-like geometry (Fig. 3c). The interatomic distances of Ba^{2+}–Se in the distorted square antiprismatic $BaSe_8$ vary from 3.2910 (12) Å to 3.4778 (17) Å. These distances are in good agreement with previously reported Ba^{2+}–Se distances of 3.305(1) Å to 3.705(1) Å in $BaSe_8$ units of $Ba_4AgGa_5Se_{12}$ [47], 3.3266(6) Å to 3.4195(6) Å in $BaCu_2SnSe_4$ [48], and 3.368(1) Å–3.745(1) Å in $BaFe_2Se_3$ [49].

3.2. Optical bandgap study of the polycrystalline $Ba_2Cu_{2.1}Ag_{1.9}Se_5$

Fig. 4 shows the Tauc plot of finely ground polycrystalline $Ba_2Cu_{2.1}Ag_{1.9}Se_5$. The bandgap of the sample can be deduced by the extrapolation method, as shown in Fig. 4, and was found in the near IR region. A direct bandgap of 1.0(2) eV was found (Fig. 4a), which is consistent with the black color of the sample. The indirect bandgap value calculated from extrapolating the linear region of the Tauc plot (Fig. 4b) of $(\alpha h\nu)^{1/2}$ vs. energy (eV) is 0.3(2) eV, which is beyond the absorption wavelength limit (~0.5 eV) of the instrument used for the study.

Thus, it is safe to conclude that the polycrystalline $Ba_2Cu_{2.1}Ag_{1.9}Se_5$ sample is a narrow bandgap semiconductor.

3.3. Temperature-dependent resistivity of the polycrystalline $Ba_2Cu_{2.1}Ag_{1.9}Se_5$

The temperature-dependent resistivity data were collected in the temperature range of 373 K – 673 K on a compressed and sintered parallelepiped-shaped pellet of $Ba_2Cu_{2.1}Ag_{1.9}Se_5$. Fig. 5 shows the variation of the electrical resistivity as a function of temperature.

The resistivity value of ~1.858 Ω cm is observed at 373 K, which lowers on raising the temperature. The lowest resistivity value of ~0.72 Ω cm was found at a maximum temperature of 673 K. The observed trend of decrease in resistivity values on heating the sample confirms its semiconducting nature. It also agrees with the bandgap study of the polycrystalline $Ba_2Cu_{2.1}Ag_{1.9}Se_5$.

3.4. Thermal conductivity and seebeck coefficient studies of $Ba_2Cu_{2.1}Ag_{1.9}Se_5$

The thermal conductivity data of the cold-pressed cylindrical sintered polycrystalline sample of $Ba_2Cu_{2.1}Ag_{1.9}Se_5$ were collected in the temperature range of 373 K – 673 K. The total thermal conductivity ($k_{total} = k_l + k_e$) of the pellet is ~0.58 W/mK at 373 K, which gradually decreases to an extremely low value of ~0.46 W/mK at 673 K (Fig. 6a).

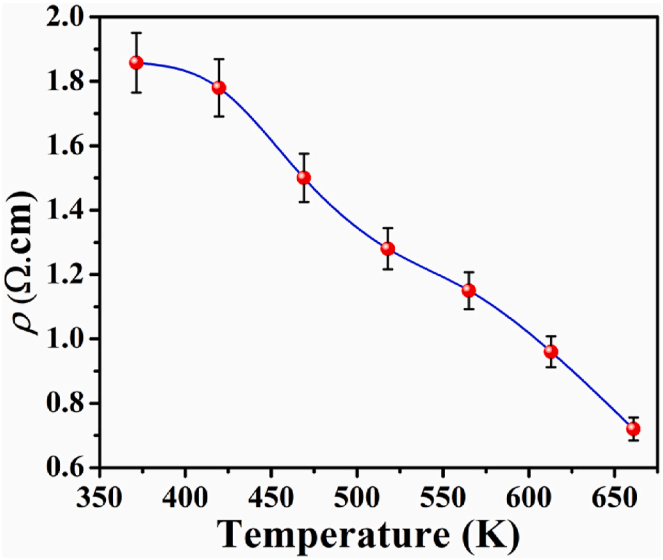

Fig. 5. The temperature-dependent electrical resistivity of the polycrystalline $Ba_2Cu_{2.1}Ag_{1.9}Se_5$ sample.

The k_l and k_e terms represent the thermal contributions from phonons and charge carriers, respectively.

Typically, the atomic vibrations of a compound increase by raising the temperature of a sample. Hence, the phonon-phonon scattering also enhances at higher temperatures, which leads to a lowering of k_l values [50]. For a semiconductor, the number of charge carriers and thus contribution of k_e to the total thermal conductivity increases on heating the sample to higher temperatures. The observed trend of total thermal conductivity with temperature suggests that the lowering of k_l values at high temperature outweighs the enhanced k_e values. Thus, the total thermal conductivity value decreases at higher temperatures. Moreover, the relatively higher electrical resistivity values (Fig. 5) of the polycrystalline $Ba_2Cu_{2.1}Ag_{1.9}Se_5$ sample suggest a minimal contribution of k_e to the k_{total} values. Thus, the k_{total} values are nearly equal to the sample's k_l values.

The observed low thermal conductivity of $Ba_2Cu_{2.1}Ag_{1.9}Se_5$ can be compared with the reported compounds such as Cu_2SnSe_4 (~0.6 W/mK) [51], $Ba_{3.2}Sn_{0.6}Bi_{2.4}S_8$ (~0.3 W/mK) [52], $Ba_4Cu_8Se_{13}$ (~0.77 W/mK) [46], and $CsSbSe_2$ (~0.3 W/mK) [53].

The variation of the Seebeck coefficient (S) with temperature is shown in Fig. 6b. The observed trend of the temperature-dependence of

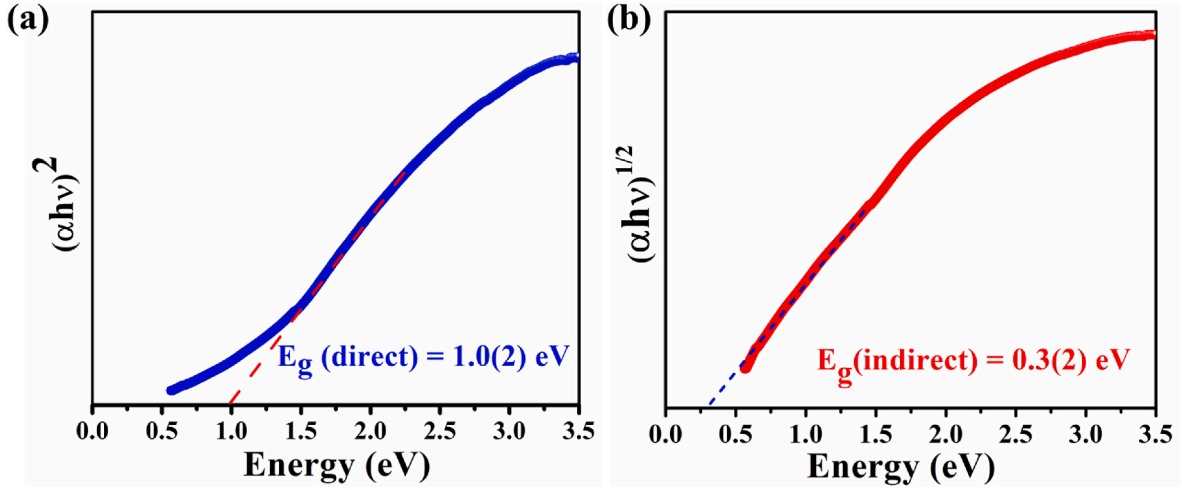

Fig. 4. The **(a)** direct bandgap and **(b)** indirect bandgap Tauc plots for the polycrystalline $Ba_2Cu_{2.1}Ag_{1.9}Se_5$ sample.

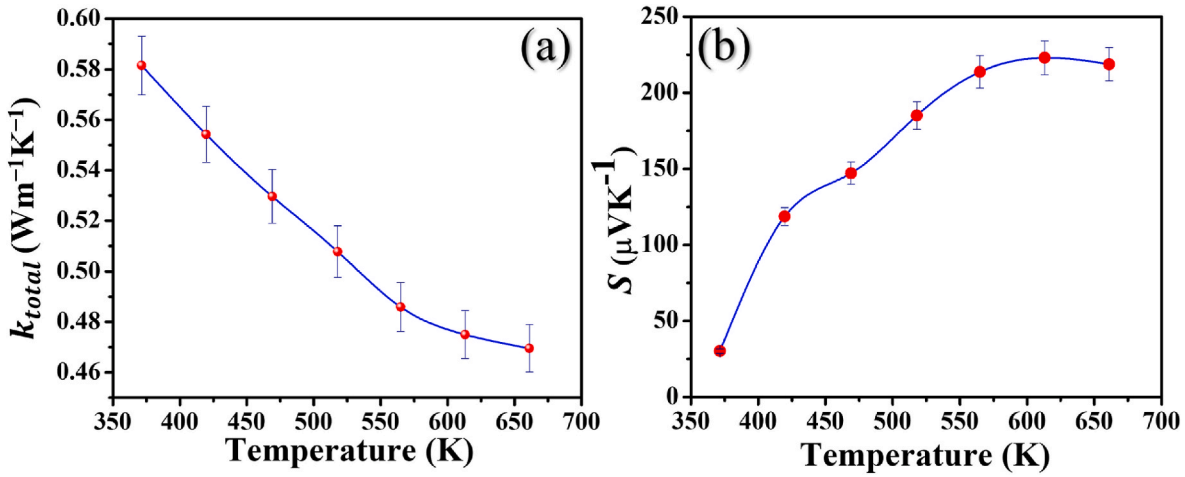

Fig. 6. (a) The variation of the total thermal conductivity and **(b)** the Seebeck coefficient values of the cold-pressed $Ba_2Cu_{2.1}Ag_{1.9}Se_5$ polycrystalline sample with temperature.

the magnitude of the S values is opposite to that of resistivity and thermal conductivity. The value of the Seebeck coefficient of the $Ba_2Cu_{2.1}Ag_{1.9}Se_5$ sample first increases on raising the temperature till 575 K, and after that, the values are almost constant, which is in contrast to the semiconducting behavior. The positive sign of the Seebeck coefficient values in the measured temperature range of 373 K – 673 K suggests that the sample is a *p*-type semiconductor with holes as predominant charge carriers. The absolute value of the Seebeck coefficient was found to be a maximum of ~220 μV K^{-1} at 673 K. The Goldsmid-Sharp bandgap equation, $E_g = 2e|S|_{max}T_{max}$ (e = elementary charge, $|S|_{max}$ = maximum magnitude of observed S value, and T_{max} = the temperature at which $|S|_{max}$ is observed), is widely used in the literature to estimate the bandgap value [54,55]. The Goldsmid bandgap value calculated from the Seebeck plot of the polycrystalline $Ba_2Cu_{2.1}Ag_{1.9}Se_5$ is about 0.3 eV which is close to the indirect bandgap of the sample (E_g = 0.3(2) eV) estimated from the Tauc plot, as shown in Fig. 4b.

Typically, the number of charge carriers is expected to increase on heating a semiconducting sample, and thus the magnitude of the S values should decrease at high temperatures. The exact reason for the observed trend of the Seebeck coefficient for the $Ba_2Cu_{2.1}Ag_{1.9}Se_5$ sample is not clear yet. Future temperature-dependent Hall studies would be useful to study the change in the number of charge carriers with temperature to understand the observed trend of the Seebeck coefficient with temperature. Similar anomalous trends of the S vs. T are known for $Cu_2ZnGeSe_{4-x}S_x$ [56] and $Bi_2Si_2Te_6$ [55]. The high electrical resistivity values of the $Ba_2Cu_{2.1}Ag_{1.9}Se_5$ sample are not favorable for *TE* applications. Future doping studies are required to increase the charge carriers to optimize the zT value for the $Ba_2Cu_{2.1}Ag_{1.9}Se_5$.

We have analyzed the microstructure of the pellet of the $Ba_2Cu_{2.1}Ag_{1.9}Se_5$ sample used for the *TE* properties by the scanning electron microscope at different magnifications (Fig. 7a–c). The reasonably dense nature of the pellet is established from these micrographs. We have not observed any preferential orientations of the grains in the pellet as well. The EDX data collected from various points and areas of the pellet showed the average composition of the sample very close to the loaded composition of the $Ba_2Cu_{2.1}Ag_{1.9}Se_5$ within 5% of the associated error.

3.5. Electrochemical performance

Many simple binary transition metal polychalcogenides [57,58] have been explored for their supercapacitor applications due to their fast ion transport, excellent flexibility, and electrical conductivity [23]. However, complex ternary and quaternary chalcogenides are mostly overlooked for this application. Therefore, we have explored the polycrystalline sample with the loaded composition of $Ba_2Cu_{2.1}Ag_{1.9}Se_5$ for energy storage supercapacitor applications. Fig. 8a presents the cyclic voltammetry (CV) curve at various scan rates 10–200 mVs^{-1}, depicting the composite electrode's pseudocapacitive behavior in 1 M KOH electrolyte.

All CV curves show a quasi-rectangular shape confirming the pseudocapacitor behavior. Furthermore, these CV curves show an increase in area under the curves by increasing the CV scan rates from 10 to 200 mVs^{-1}, explaining the better charge storage ability of the material for supercapacitor application [37,38,59]. The GCD cyclings were conducted to examine the charge storage nature of the material by applying various current densities, as shown in Fig. 8b–c. The $Ba_2Cu_{2.1}Ag_{1.9}Se_5$ composite electrode delivers a specific capacitance of 86, 76, 57, 43, 32, and 20 F g^{-1} at applied current densities of 0.25, 0.5, 1, 2, 3, and 5 Ag^{-1}, respectively. Cycling stability is the vital parameter of any supercapacitor, showing potential for practical applications. The cycle-life was examined by continuous GCD processes at 100 mVs^{-1}, as shown in Fig. 8d. The material is stable over 10,000 cycles with a capacitance retention of 85% after cycling in a 1 M KOH system.

Further, to understand the charge storage nature, the impedance study was carried out before cycling, after the 1st cycle, after the 5000th

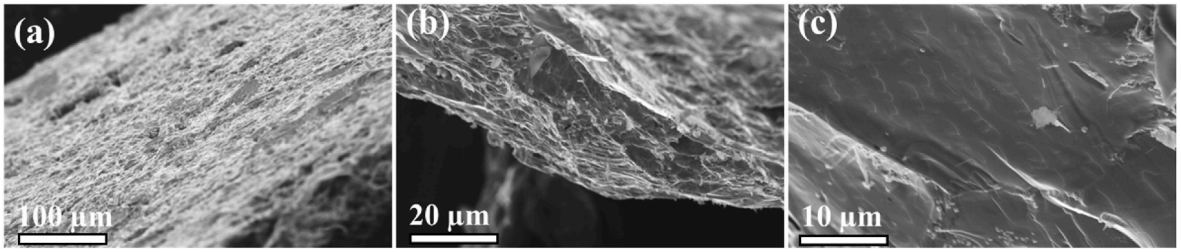

Fig. 7. (a–c) The SEM cross-sectional images of the fracture pellet of the polycrystalline $Ba_2Cu_{2.1}Ag_{1.9}Se_5$ sample at different magnifications.

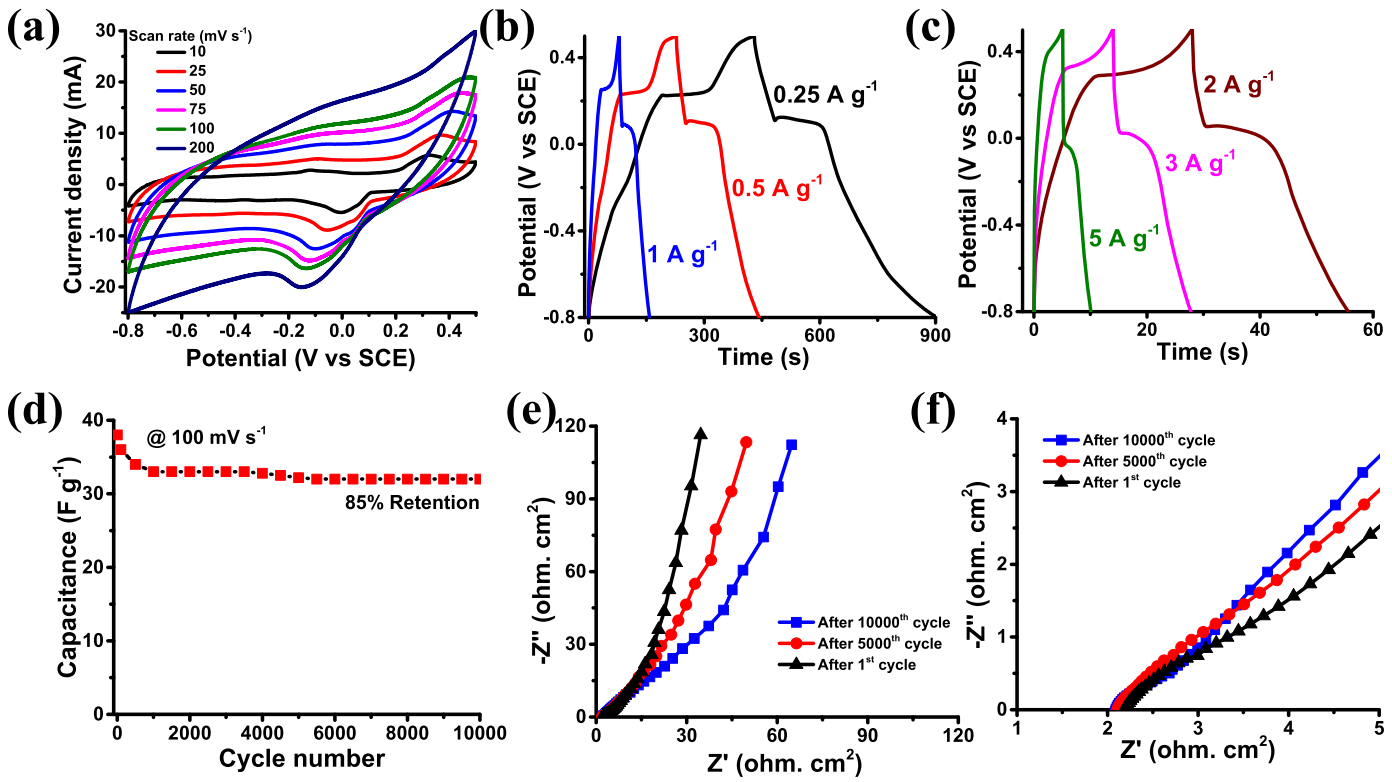

Fig. 8. Electrochemical characterizations of the polycrystalline $Ba_2Cu_{2.1}Ag_{1.9}Se_5$: (a) the CV curves at various scan rates, (b–c) Galvanostatic charge-discharge at various current densities, (d) the cycle-life studies at 100 mVs^{-1} for 10,000 cycles, (e) the electrochemical impedance spectra after 1st, 5000th and 10000th galvanostatic charge-discharge cycles in the frequency range between 1 MHz and 10 mHz, and (f) the high-frequency region of Fig. 8e.

cycle, and after the 10000th cycle, as presented in Fig. 8e. The impedance plot shows no change in the equivalent series resistance in the high-frequency region (Fig. 8f) with the increase in cycling. But charge storage behavior decreases by continuous cycling (Fig. 8e) as the EIS curves move away from Y-axis (− Z′′ imaginary axis) at the low-frequency region. A thorough understanding of the martial and further developments are desired to improve specific capacitance. Nevertheless, $Ba_2Cu_{2.1}Ag_{1.9}Se_5$ opens up a new dimension of electrode material for supercapacitors.

4. Conclusions

The single crystals and polycrystalline phase of $Ba_2Cu_{2.1(1)}Ag_{1.9(1)}Se_5$ were successfully synthesized by the high-temperature sealed tube method. The $Ba_2Cu_{2.1(1)}Ag_{1.9(1)}Se_5$ crystallizes in the monoclinic crystal system with cell constants of $a = 16.0342(15)$ Å, $b = 4.4162(4)$ Å, $c = 9.1279(9)$ Å, $\beta = 124.005\ (2)^{\circ}$, and $V = 535.82(9)$ Å^3. The asymmetric unit of $Ba_2Cu_{2.1(1)}Ag_{1.9(1)}Se_5$ structure contains six independent crystallographic sites: one Ba1, one *M*1, one *M*2, and three Se sites (Se1, Se2, and Se3). The Cu and Ag atoms are disordered at both *M*1 and *M*2 sites. The optical bandgap of the polycrystalline $Ba_2Cu_{2.1}Ag_{1.9}Se_5$ sample was found to be 1.0(2) eV. The cold-pressed sintered polycrystalline sample also shows an extremely low thermal conductivity of ~0.46 W/mK at 673 K. The positive sign of the Seebeck coefficient indicates the *p*-type semiconducting nature of the material. The temperature-dependent resistivity data supports the optical bandgap study of the polycrystalline sample and confirms the semiconducting nature of the material. Further, electrochemical studies of the polycrystalline $Ba_2Cu_{2.1}Ag_{1.9}Se_5$ suggest that it could be a potential electrode material for supercapacitors.

Credit author statement

GP and SJ carried out the synthesis, crystal structure determinations, powder X-ray diffraction studies, EDX analysis, and UV–Vis–NIR diffuse reflectance measurements. SKM and SM have carried out the Electrochemical property study. All authors contributed to the final manuscript. After getting input from all authors, GP, SM, and JP wrote the manuscript. JP was involved in conceptualization, overall guidance, data analysis, writing, reviewing, and editing the manuscript.

Declaration of competing interest

The authors declare that they have no known competing financial interests or personal relationships that could have appeared to influence the work reported in this paper.

Data availability

Data will be made available on request.

Acknowledgments

JP thanks DST-SERB, the Government of India (GOI) for the financial support under the core research (CRG) grant (Grant number: CRG/2021/003641) and ECR grant (ECR/2017/000822), and IIT Hyderabad for seed grant and research facilities. GP, SJ, and SM thank the Ministry of Education (MOE), GOI, and IIT Hyderabad for the research fellowships. The authors also gratefully acknowledge DST-FIST (SR/FST/ETI-421/2016) for the SEM-EDX facility.

Appendix A. Supplementary data

Supplementary data to this article can be found online at https://doi.org/10.1016/j.solidstatesciences.2023.107115.

References

[1] A. Assoud, J. Xu, H. Kleinke, Structures and physical properties of new semiconducting polyselenides $Ba_2Cu_\delta Ag_{4-\delta}Se_5$ with unprecedented linear Se_3^{4-} units, Inorg. Chem. 46 (2007) 9906–9911, https://doi.org/10.1021/ic701278b.

[2] S. Jana, M. Ishtiyak, A. Mesbah, S. Lebègue, J. Prakash, C.D. Malliakas, J.A. Ibers, Synthesis and characterization of $Ba_2Ag_2Se_2(Se_2)$, Inorg. Chem. 58 (2019) 7837–7844, https://doi.org/10.1021/acs.inorgchem.9b00506.

[3] S.A. Sunshine, J.A. Ibers, Redetermination of the structures of $CuTaS_3$ and Nb_2Se_9, Acta Crystallogr. C 43 (1987) 1019–1022, https://doi.org/10.1107/S0108270187093168.

[4] A. Assoud, S. Thomas, B. Sutherland, H. Zhang, T.M. Tritt, H. Kleinke, Thermoelectric properties of the new polytelluride $Ba_3Cu_{14-\delta}Te_{12}$, Chem. Mater. 18 (2006) 3866–3872, https://doi.org/10.1021/cm060776k.

[5] R. Chetty, P.K.D. S, G. Rogl, P. Rogl, E. Bauer, H. Michor, S. Suwas, S. Puchegger, G. Giester, R.C. Mallik, Thermoelectric properties of a Mn substituted synthetic tetrahedrite, Phys. Chem. Chem. Phys. 17 (2014) 1716–1727, https://doi.org/10.1039/C4CP04039B.

[6] M. Oudah, K.M. Kleinke, H. Kleinke, Thermoelectric properties of the quaternary chalcogenides $BaCu_{5.9}STe_6$ and $BaCu_{5.9}SeTe_6$, Inorg. Chem. 54 (2015) 845–849, https://doi.org/10.1021/ic502055z.

[7] Z. Guo, F. Sun, W. Yuan, Chemical intercalations in layered transition metal chalcogenides: syntheses, structures, and related properties, Cryst, Growth Des. 17 (2017) 2238–2253, https://doi.org/10.1021/acs.cgd.7b00146.

[8] J. Guo, S. Jin, G. Wang, S. Wang, K. Zhu, T. Zhou, M. He, X. Chen, Superconductivity in the iron selenide $K_xFe_2Se_2$ ($0 \leq x \leq 1.0$), Phys. Rev. B 82 (2010), 180520, https://doi.org/10.1103/PhysRevB.82.180520.

[9] B.T. Matthias, M. Marezio, E. Corenzwit, A.S. Cooper, H.E. Barz, High-temperature superconductors, the first ternary system, Science 175 (1972) 1465–1466, https://doi.org/10.1126/science.175.4029.1465.

[10] Q.-G. Mu, B.-B. Ruan, K. Zhao, B.-J. Pan, T. Liu, L. Shan, G.-F. Chen, Z.-A. Ren, Superconductivity at 10.4 K in a novel quasi-one-dimensional ternary molybdenum pnictide $K_2Mo_3As_3$, Sci. Bull. 63 (2018) 952–956, https://doi.org/10.1016/j.scib.2018.06.011.

[11] M. Sturza, J.M. Allred, C.D. Malliakas, D.E. Bugaris, F. Han, D.Y. Chung, M. G. Kanatzidis, Tuning the magnetic properties of new layered iron chalcogenides $(BaF)_2Fe_{2-x}Q_3$ (Q = S, Se) by changing the defect concentration on the iron sublattice, Chem. Mater. 27 (2015) 3280–3290, https://doi.org/10.1021/acs.chemmater.5b00287.

[12] I.E. Grey, H. Steinfink, Crystal structure of Ba_2MnSe_3. Linear antiferromagnetism in Ba_2MnX_3 (X = S, Se), Inorg. Chem. 10 (1971) 691–696, https://doi.org/10.1021/ic50098a007.

[13] J. Joshi, H.M. Hill, S. Chowdhury, C.D. Malliakas, F. Tavazza, U. Chatterjee, A.R. H. Walker, P.M. Vora, Short-range charge density wave order in 2H-TaS_2, Phys. Rev. B 99 (2019), 245144, https://doi.org/10.1103/PhysRevB.99.245144.

[14] G. Giuffredi, T. Asset, Y. Liu, P. Atanassov, F.D. Fonzo, Transition metal chalcogenides as a versatile and tunable platform for catalytic CO_2 and N_2 electroreduction, ACS Mater. Au 1 (2021) 6–36, https://doi.org/10.1021/acsmaterialsau.1c00006.

[15] I. Chung, M.G. Kanatzidis, Metal chalcogenides: a rich source of nonlinear optical materials, Chem. Mater. 26 (2014) 849–869, https://doi.org/10.1021/cm401737s.

[16] D.M. Rowe, Modules, Systems, and Applications in Thermoelectrics, CRC Press, 2012.

[17] H. Liu, F. Xu, L. Zhang, W. Zhang, L. Chen, Q. Li, C. Uher, T. Day, G.J. Snyder, Copper ion liquid-like thermoelectrics, Nat. Mater. 11 (2012) 422–425, https://doi.org/10.1038/nmat3273.

[18] T. Ghosh, S. Roychowdhury, M. Dutta, K. Biswas, High-performance thermoelectric energy conversion: a tale of atomic ordering in $AgSbTe_2$, ACS Energy Lett. 6 (2021) 2825–2837, https://doi.org/10.1021/acsenergylett.1c01184.

[19] M.A. McGuire, A.F. May, D.J. Singh, M.-H. Du, G.E. Jellison, Transport and optical properties of heavily hole-doped semiconductors $BaCu_2Se_2$ and $BaCu_2Te_2$, J. Solid State Chem. 184 (2011) 2744–2750, https://doi.org/10.1016/j.jssc.2011.08.021.

[20] A. Assoud, S. Thomas, B. Sutherland, H. Zhang, T.M. Tritt, H. Kleinke, Thermoelectric properties of the new polytelluride $Ba_3Cu_{14-\delta}Te_{12}$, Chem. Mater. 18 (2006) 3866–3872, https://doi.org/10.1021/cm060776k.

[21] G. Tan, S. Hao, J. Zhao, C. Wolverton, M.G. Kanatzidis, High thermoelectric performance in electron-doped $AgBi_3S_5$ with ultralow thermal conductivity, J. Am. Chem. Soc. 139 (2017) 6467–6473, https://doi.org/10.1021/jacs.7b02399.

[22] L. Pan, D. Bérardan, N. Dragoe, High thermoelectric properties of n-type $AgBiSe_2$, J. Am. Chem. Soc. 135 (2013) 4914–4917, https://doi.org/10.1021/ja312474n.

[23] D. Zhang, L. Li, Y. Zhang, Metal chalcogenides-based materials for high-performance metal ion capacitors, J. Alloys Compd. 869 (2021), 159352, https://doi.org/10.1016/j.jallcom.2021.159352.

[24] S. Jana, M. Ishtiyak, G. Panigrahi, J. Prakash, A. Mesbah, S. Gueddida, S. Lebègue, C.D. Malliakas, J.A. Ibers, Ternary chalcogenides BaM_xTe_2 (M = Cu, Ag): syntheses, modulated crystal structures, optical properties, and electronic calculations, Inorg. Chem. 59 (2020) 12276–12285, https://doi.org/10.1021/acs.inorgchem.0c01319.

[25] M. Ishtiyak, S. Jana, R. Karthikeyan, M. Ramesh, B. Tripathy, S.K. Malladi, M. K. Niranjan, J. Prakash, Syntheses of five new layered quaternary chalcogenides $SrScCuSe_3$, $SrScCuTe_3$, $BaScCuSe_3$, $BaScCuTe_3$, and $BaScAgTe_3$: crystal structures, thermoelectric properties, and electronic structures, Inorg. Chem. Front. 8 (2021) 4086–4101, https://doi.org/10.1039/D1QI00717C.

[26] S. Barman, S. Jana, G. Panigrahi, S. Yadav, M.K. Niranjan, J. Prakash, $Ba_3Zr_2Cu_4S_9$: the first quaternary phase of the Ba–Zr–Cu–S system, New J. Chem. 46 (2022) 15976–15986, https://doi.org/10.1039/D2NJ02972C.

[27] APEX3, Program for Data Collection on Area Detectors, Bruker AXS Inc., Madison, WI, USA, 2016.

[28] G.M. Sheldrick, SADABS, Department of Structural Chemistry, University of Göttingen: Göttingen, Germany, 2008.

[29] G.M. Sheldrick, Crystal structure refinement with *SHELXL*, Acta Crystallogr. C 71 (2015) 3–8, https://doi.org/10.1107/S2053229614024218.

[30] G.M. Sheldrick, XPREP Version 2008/2, Bruker AXS Inc., Madison, 2008.

[31] G.M. Sheldrick, A short history of *SHELX*, Acta Crystallogr. A 64 (2008) 112–122, https://doi.org/10.1107/S0108767307043930.

[32] A.L. Spek, Single-crystal structure validation with the program *PLATON*, J. Appl. Crystallogr. 36 (2003) 7–13, https://doi.org/10.1107/S0021889802022112.

[33] L.M. Gelato, E. Parthé, *Structure TIDY* – a computer program to standardize crystal structure data, J. Appl. Crystallogr. 20 (1987) 139–143, https://doi.org/10.1107/S0021889887086965.

[34] Match3! - Phase Analysis Using Powder Diffraction. https://www.crystalimpact.com/match/.

[35] G. Kortüm, Reflectance Spectroscopy, Springer, New York, 1969.

[36] E.I. Andritsos, E. Zarkadoula, A.E. Phillips, M.T. Dove, C.J. Walker, V.V. Brazhkin, K. Trachenko, Heat capacity of matter beyond the Dulong-Petit value, J. Phys. Condens. Matter 25 (2013), 235401, https://doi.org/10.1088/0953-8984/25/23/235401.

[37] Z. Yu, L. Tetard, L. Zhai, J. Thomas, Supercapacitor electrode materials: nanostructures from 0 to 3 dimensions, Energy Environ. Sci. 8 (2015) 702–730, https://doi.org/10.1039/C4EE03229B.

[38] S. Muduli, S.K. Pati, S. Swain, S.K. Martha, MoO_3@ZnO nanocomposite as an efficient anode material for supercapacitors: a cost effective synthesis approach, Energy Fuels 35 (2021) 16850–16859, https://doi.org/10.1021/acs.energyfuels.1c01665.

[39] A.A. Coelho, *TOPAS* and *TOPAS-Academic*: an optimization program integrating computer algebra and crystallographic objects written in C++, J. Appl. Crystallogr. 51 (2018) 210–218, https://doi.org/10.1107/S1600576718000183.

[40] W.L. Bragg, XLII. The crystalline structure of copper, Lond. Edinb. Dublin Philos. Mag. J. Sci. 28 (1914) 355–360, https://doi.org/10.1080/14786440908635219.

[41] A. Martínez, Bonding interactions of metal clusters [M_n (M= Cu, Ag, Au; n=1-4)] with ammonia. Are the metal clusters adequate as a model of surfaces? J. Braz. Chem. Soc. 16 (2005) 337–344, https://doi.org/10.1590/S0103-50532005000300007.

[42] P. Böttcher, Darstellung und Kristallstruktur der Dialkalimetalltrichalkogenide Rb_2S_3, Rb_2Se_3, Cs_2S_3 und Cs_2Se_3, Z. Anorg. Allg. Chem. 461 (1980) 13–21, https://doi.org/10.1002/zaac.19804610103.

[43] J. Prakash, S. Stoyko, L. Voss, S. Bobev, On the extended series of quaternary Zintl phases $Ca_{13}RE MnSb_{11}$ (RE = La–Nd, Sm, Gd–Dy), Eur. J. Inorg. Chem. 2016 (2016) 2912–2922, https://doi.org/10.1002/ejic.201600306.

[44] P. Dürichen, M. Bolte, W. Bensch, Synthesis, crystal structure, and properties of polymeric $Rb_{12}Nb_6Se_{35}$, a novel ternary niobium selenide consisting of infinite anionic chains built up by Nb_2Se_{11} Units containing an uncommon Se_3^{4-}-fragment, J. Solid State Chem. 140 (1998) 97–102, https://doi.org/10.1006/jssc.1998.7869.

[45] Y. Lu, J.A. Ibers, Synthesis and characterization of the new quaternary one-dimensional chain materials, potassium copper niobium selenides, $K_2CuNbSe_4$ and $K_3CuNb_2Se_{12}$, Inorg. Chem. 30 (1991) 3317–3320, https://doi.org/10.1021/ic00017a018.

[46] S. Maier, O. Perez, D. Pelloquin, D. Berthebaud, S. Hébert, F. Gascoin, Linear, hypervalent Se_3^{4-} units and unprecedented Cu_4Se_9 building blocks in the copper(I) selenide $Ba_4Cu_8Se_{13}$, Inorg. Chem. 56 (2017) 9209–9218, https://doi.org/10.1021/acs.inorgchem.7b01224.

[47] W. Yin, K. Feng, D. Mei, J. Yao, P. Fu, Y. Wu, Ba_2AgInS_4 and $Ba_4MGa_5Se_{12}$ (M = Ag, Li): syntheses, structures, and optical properties, Dalton Trans. 41 (2012) 2272–2276, https://doi.org/10.1039/C2DT11895E.

[48] A. Assoud, N. Soheilnia, H. Kleinke, New quaternary barium copper/silver selenostannates: different coordination spheres, Metal−Metal interactions, and physical properties, Chem. Mater. 17 (2005) 2255–2261, https://doi.org/10.1021/cm050102u.

[49] H.Y. Hong, H. Steinfink, The crystal chemistry of phases in the Ba–Fe–S and Se systems, J. Solid State Chem. 5 (1972) 93–104, https://doi.org/10.1016/0022-4596(72)90015-1.

[50] D.T. Morelli, V. Jovovic, J.P. Heremans, Intrinsically minimal thermal conductivity in cubic I−V−VI_2 semiconductors, Phys. Rev. Lett. 101 (2008), 035901, https://doi.org/10.1103/PhysRevLett.101.035901.

[51] W. Li, S. Lin, X. Zhang, Z. Chen, X. Xu, Y. Pei, Thermoelectric properties of Cu_2SnSe_4 with intrinsic vacancy, Chem. Mater. 28 (2016) 6227–6232, https://doi.org/10.1021/acs.chemmater.6b02416.

[52] S. Jana, G. Panigrahi, B. Tripathy, S.K. Malladi, M.K. Niranjan, J. Prakash, A new non-stoichiometric quaternary sulfide $Ba_{3.14(4)}Sn_{0.61(1)}Bi_{2.39(1)}S_8$: synthesis, crystal structure, physical properties, and electronic structure, J. Solid State Chem. 308 (2022), 122914, https://doi.org/10.1016/j.jssc.2022.122914.

[53] S. Mukhopadhyay, D.J. Singh, T.L. Reinecke, Ultralow thermal conductivity in Cs–Sb–Se compounds: lattice instability versus lone-pair electrons, Chem. Mater. 32 (2020) 8906–8913, https://doi.org/10.1021/acs.chemmater.0c02688.

[54] H.J. Goldsmid, J.W. Sharp, Estimation of the thermal band gap of a semiconductor from Seebeck measurements, J. Electron. Mater. 28 (1999) 869–872, https://doi.org/10.1007/s11664-999-0211-y.

[55] Y. Luo, Z. Ma, S. Hao, S. Cai, Z.-Z. Luo, C. Wolverton, V.P. Dravid, J. Yang, Q. Yan, M.G. Kanatzidis, Thermoelectric performance of the 2D $Bi_2Si_2Te_6$ semiconductor, J. Am. Chem. Soc. 144 (2022) 1445–1454, https://doi.org/10.1021/jacs.1c12507.

[56] W.G. Zeier, C.P. Heinrich, T. Day, C. Panithipongwut, G. Kieslich, G. Brunklaus, G. J. Snyder, W. Tremel, Bond strength dependent superionic phase transformation in

the solid solution series $Cu_2ZnGeSe_{4-x}S_x$, J. Mater. Chem. 2 (2014) 1790–1794, https://doi.org/10.1039/C3TA13007J.

[57] T. Zhu, H.B. Wu, Y. Wang, R. Xu, X.W. (David) Lou, Formation of 1D hierarchical structures composed of Ni_3S_2 nanosheets on CNTs backbone for supercapacitors and photocatalytic H_2 production, Adv. Energy Mater. 2 (2012) 1497–1502, https://doi.org/10.1002/aenm.201200269.

[58] J. Theerthagiri, K. Karuppasamy, G. Durai, A.U.H.S. Rana, P. Arunachalam, K. Sangeetha, P. Kuppusami, H.-S. Kim, Recent advances in metal chalcogenides (*MX; X* = S, Se) nanostructures for electrochemical supercapacitor applications: a brief review, Nanomaterials 8 (2018) 256, https://doi.org/10.3390/nano8040256.

[59] M. Salanne, B. Rotenberg, K. Naoi, K. Kaneko, P.-L. Taberna, C.P. Grey, B. Dunn, P. Simon, Efficient storage mechanisms for building better supercapacitors, Nat. Energy 1 (2016) 1–10, https://doi.org/10.1038/nenergy.2016.70.